PAPER

Check for updates

Water-resistant organic–inorganic hybrid perovskite quantum dots activated by the electron-deficient d-orbital of platinum atoms for nitrogen fixation†

Yixuan Gao,‡[a] Xiao Su,‡[a] Juanjuan Wei,‡[a] Jianghui Sun,[a] Min Zhang,[a] Hongwei Tan, [ID] *[a] Jiangwei Zhang, [ID] *[b] Jin Ouyang [ID] [a] and Na Na [ID] *[a]

Due to their special physicochemical properties, organic–inorganic hybrid perovskite quantum dots (OIP QDs) are ideal and potential catalysts for the nitrogen reduction reaction (NRR). However, the OIP QD-based NRR is limited by poor water resistance, competitive suppression by the hydrogen evolution reaction, and inefficient active sites on the catalyst surfaces. Herein, to ensure an efficient NRR in aqueous solution, a water-resistant polycarbonate-part-encapsulated heterojunction of Zn,Pt^{IV} co-doped PbO-MAPbBr$_3$ (Pt^{IV}/Zn/PbO/PC-Zn/MAPbBr$_3$) is prepared through one-step electrospray-based micro-droplet synthesis. Confirmed by both experimental and theoretical examinations, PbO is exposed on the PC-part-encapsulated surface to construct a Type I heterojunction. This heterojunction is further improved by synergistic co-doping with Pt^{IV} to facilitate efficient electron transfer for efficient photocatalysis of the NRR. Due to the active sites of the d-orbital electron-deficient Pt atoms (exhibiting a lower reaction energy barrier and highly selective N$_2$ adsorption), the ammonia yield rate is 40 times higher than that without doping. This work initiates and develops on the application of OIP QDs in the NRR.

1. Introduction

Organic–inorganic hybrid perovskite materials have received great attention due to their special physicochemical properties.[1–7] Due to their high extinction coefficients,[8] wide absorption ranges,[9] high carrier mobilities[10–12] and tunable bandgaps,[13] organic–inorganic hybrid perovskites quantum dots (OIP QDs) are ideal and potential photocatalytic reduction agents.[14,15] However, the inherent poor water resistance becomes a major hindrance for OIP QD applications.[9,16] Taking methylammonium lead bromide (MAPbBr$_3$, MA: CH$_3$NH$_3$) OIP QDs as an example, MA is structurally located in the interstitial center of the networks of corner-sharing PbBr$_6$ octahedra.[17–20] However, water can weaken the interaction between MA and the PbBr$_6$ octahedra *via* hydrogen bonding

with the crystal lattice of MAPbBr$_3$.[9,17,21,22] Consequently, the present photocatalytic reduction of OIP QDs is mainly focused on photocatalytic H$_2$ evolution and CO$_2$ reduction in non-aqueous media.[9,23–29] The application of MAPbBr$_3$ in nitrogen fixation by the nitrogen reduction reaction (NRR) in water is yet to be developed.

To improve the water resistance of OIP QDs, encapsulations using hydrophobic polymer matrices, AlO$_x$-passivated films or SiO$_2$ coating core–shell structures have been reported.[30] However, these encapsulations are not feasible for NRR due to the insulating shells restricting charge transport, which is crucial for photocatalytic reductions.[31,32] The microdroplet reaction has been newly developed for fast synthesis and nanoparticle preparation, which is achieved by spraying charged droplets for accelerated reactions. In particular, water-resistant encapsulations of OIP QDs by polymers can be obtained.[33] However, polymer encapsulation results in transport restriction, which restricts the wider application of OIP QDs.[34–36] Consequently, the NRR performance catalyzed by OIP QDs is still limited due to the following reasons. (1) The competing hydrogen evolution reaction (HER) seriously limits the production selectivity and yield rate of NH$_3$ in the NRR.[37–39] This is due to the high favorability of electron transfer for the HER as well as the preferential adsorption of H atoms over N$_2$

[a]*Key Laboratory of Radiopharmaceuticals, Ministry of Education, College of Chemistry, Beijing Normal University, Beijing 100875, China. E-mail: nana@bnu.edu.cn, hongwei.tan@bnu.edu.cn*
[b]*Dalian National Laboratory for Clean Energy & State, Key Laboratory of Catalysis, Dalian Institute of Chemical Physics, Chinese Academy of Sciences (CAS), China. E-mail: zjw11@tsinghua.org.cn*
†Electronic supplementary information (ESI) available. See DOI: https://doi.org/10.1039/d2nr02662g
‡These authors contributed equally to this work.

molecules.[40] (2) The intrinsic catalytic activity of the active metal centers on the catalyst surface is inefficient.[41,42] This arises from the weak affinity of N_2 to the catalysts, which lack electron deficient sites to accept the lone pair electrons of N_2.[43] Therefore, further surface engineering of OIP QD structures is expected to overcome the traditionally favored H adsorption and improve the intrinsic photocatalytic activity towards the NRR.[44–46]

An emerging strategy to kinetically boost the NRR performance is by creating electron deficient catalytic sites *via* electronic structure modifications on active metal centers.[47–49] For instance, the transition metal Pt has exhibited an effective way to improve the activity and selectivity toward HER.[50–52] However, the NRR of Pt element was normally suppressed by HER competition, which excessively adsorbed H atoms to occupy the active sites instead of N_2 activation.[37,53] This is normally generated from the strong Pt–H interaction (unfulfilled 5d orbitals of Pt with the s orbital of H) because the metal d-band states are close to the Fermi level (E_f).[54–56] In fact, the adsorption on the catalysts can be tailored by tuning the d orbitals of the transition metals.[57] Therefore, the selectivity of NRR would be improved by rationally controlling the microstructure and electronic properties of photocatalysts.[41,58] Consequently, for selective NRR, the ideal catalysts of OIP QDs should be further designed with (1) a lower d-band state to weaken H adsorption and (2) abundant electron deficient sites with strong N_2 affinity.[54,59–61]

Herein, a water-resistant OIP QDs was rapidly prepared by the one-step ESI-based microdroplet synthesis in microseconds, termed as polycarbonate (PC)-part-encapsulated Zn, Pt^{IV}-codoped PbO-MAPbBr$_3$ heterojunction (Pt^{IV}/Zn/PbO/PC-Zn/MAPbBr$_3$). During the fast ESI, the core of Zn/MAPbBr$_3$ was crystallized, followed by PC encapsulation to obtain good water-resistance without environmental pollution. In this rapid process, Zn/PbO was exposed on the surface through the substitution of Zn by the internal Pb of MAPbBr$_3$, which resulted in a heterojunction. Significantly, this heterojunction was further improved by co-doping with Pt^{IV}, which obtained Zn, Pt^{IV}-co-doped PbO-MAPbBr$_3$. Therefore, the Pt^{IV}/Zn co-doped PbO acted as a shell on Pt^{IV}/Zn/PbO/PC-Zn/MAPbBr$_3$, forming an improved heterojunction with a straddling gap (Type I) for NRR. Compared to lower valent Pt^{II}-doped materials (Pt^{II}/Zn/PbO), the Pt^{IV}/Zn/PbO species created electron-deficient sites with strong affinity toward N_2 and suppressed H adsorption. Consequently, the metal atom was positively charged with high-valence states, which improved electron delocalization of Pt^{IV} d-orbitals for electron transfer to N_2. Simultaneously, the electron deficient sites of Pt^{IV} lowered d-band center to inhibit H adsorption, while it enhanced the affinity toward N_2 to suppress HER. The preferential N_2 adsorption over H atom at electron deficient sites was further confirmed by the density functional theory (DFT) calculations. The Pt^{IV}/Zn/PbO/PC-Zn/MAPbBr$_3$ exhibited a higher ammonia production rate than the single Zn-doped one, which was 40 times higher than that without doping.

2. Experimental

2.1 Synthesis of PC-part-encapsulated Zn,Pt^{IV}-codoped PbO-MAPbBr$_3$ heterojunction

Polycarbonate resin (PC, M.W. 45 000, Acros), methylamine hydrobromide (CH$_3$NH$_3$Br, MABr, 98%, Innochem), lead(II) bromide (PbBr$_2$, Puratronic, 99.9%, Macklin), N,N-dimethylformamide (DMF, 99.9%, extra dry, Innochem), H$_2$PtCl$_6$ (99.9%, Macklin), K$_2$PtCl$_4$ (99.9%, Macklin), and C$_4$H$_8$O$_4$Zn (Macklin, AR). Ultrapure water (Mill-Q, Millipore, 18.2 MΩ) was used in all experiments. All chemicals were used without further purification.

The synthesis of polycarbonate-part-encapsulated Zn,Pt^{IV} co-doped PbO-MAPbBr$_3$ (Pt^{IV}/Zn/PbO/PC-Zn/MAPbBr$_3$) was accomplished by one-step electrospray (ESI) microdroplet synthesis. As shown in Scheme 1a, the DMF solution containing PC, CH$_3$NH$_3$Br (MABr), C$_4$H$_8$O$_4$Zn, H$_2$PtCl$_6$, and PbBr$_2$ was fed into a centrifuge tube, whose flow rate was controlled by the fluxion mixture of N_2 and O_2 (160 L min^{-1}). The electrospray voltage of the DC voltage was +20 kV (Scheme 1a). Therefore, the sprayed electropositive droplets containing Pt^{IV}/Zn/PbO/PC-Zn/MAPbBr$_3$ products were collected on a conical flask receptor attached to a negative electrode. Finally, the yellow dry Pt^{IV}/Zn/PbO/PC-Zn/MAPbBr$_3$ nanocatalyst on the receptor was then dispersed in ultrapure water. Subsequently, the mixture was centrifuged under 7000 rpm for 10 min to collect the precipitate. After that, the obtained yellow dry Pt^{IV}/Zn/PbO/PC-Zn/MAPbBr$_3$ products were dispersed in ethanol.

2.2 Characterization

High voltage was supplied by a DC high-voltage power supply (China, HB-Z303-1AC). Transmission electron microscopy (TEM) imaging was performed on an FEI Talos 200 s TEM with an operating voltage of 200 kV. X-ray diffraction measurement was performed with a Maxima XRD-7000 (Shimadzu, Japan). The Fourier transform infrared (FT-IR) spectra of the samples were recorded on a PerkinElmer TGA 7 infrared spectrometer to identify the functional groups on the surface of all the samples. Raman spectra were recorded at room temperature using a Raman spectrometer (Renishaw RM-1000) in a back-scattering geometry with a 532 nm laser as the excitation source. The XPS spectra were recorded using a PHI-5300 ESCA spectrometer (PerkinElmer) equipped with an Al Kα excitation source. Photoluminescence spectroscopy measurements were employed by an FLS980 fluorescence spectrophotometer. The photocurrent and electrochemical impedance spectra were acquired with an electrochemical workstation (CHI 660e). The work functions in the Pt^{IV}/Zn/PbO and Zn/MAPbBr$_3$ were investigated using ultraviolet photoemission spectroscopy (UPS, AXIS-Nova).

2.3 X-ray absorption fine structure spectra measurements

The X-ray absorption fine structure spectra (XAFS) of the Pb, Zn, and Pt K-edge was collected at the 1 W1B beamline of Beijing Synchrotron Radiation Facility (BSRF). The EXAFS spectra were obtained by subtracting the post-edge background
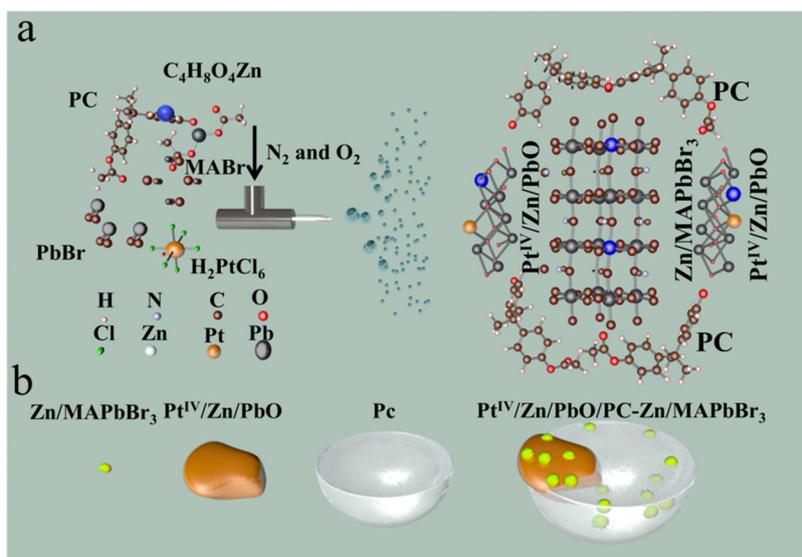
Scheme 1 The preparation of the $Pt^{IV}/Zn/PbO/PC-Zn/MAPbBr_3$ heterojunction materials. (a) A schematic illustration of the ESI-based microdroplet synthesis. (b) A schematic image of the structure.

from the overall absorption and then normalized with respect to the edge-jump step. Subsequently, the $\chi(k)$ data was Fourier transformed to real (R) space to separate the EXAFS contributions from different coordination shells. To obtain the quantitative structural parameters around the central atoms, least-squares curve parameter fitting was performed using the Artemis module. The following EXAFS equation was used for the calculation of the theoretical scattering amplitudes, phase shifts, and the photoelectron mean free paths.

$$\chi(k) = \sum_j \frac{N_j S_0^2 F_j(k)}{kR_j^2} \exp[-2k^2\sigma_j^2] \exp\left[\frac{-2R_j}{\lambda(k)}\right] \sin[2kR_j + \Phi_j(k)]$$

(1)

R_j is the distance between the X-ray absorbing central atom and the atoms in the jth atomic shell (backscatterer), N_j is the number of neighbors in the jth atomic shell, S_0^2 is the amplitude reduction factor, $F_j(k)$ is the effective curved-wave backscattering amplitude, λ is the mean free path in Å, $\phi_j(k)$ is the phase shift (including the phase shift for each shell and the total central atom phase shift), and σ_j is the Debye–Waller parameter of the jth atomic shell (variation of distances around the average R_j). The functions $F_j(k)$, λ, and $\phi_j(k)$ were calculated with the *ab initio* code FEFF9. Additional details for EXAFS simulations are given below. All fits were performed in the R space with a k-weight of 2 for the Zn K-edge, Pb K-edge, and Pt K-edge. The obtained S_0^2 was fixed in the subsequent fitting, which made the internal atomic distances R, the Debye–Waller factor σ^2, and the edge-energy shift ΔE^0 run freely.

2.4 Photocatalytic N$_2$ reduction reaction measurements

The photocatalytic N$_2$ reduction reaction (NRR) performances of the photocatalysts were evaluated in a photocatalytic reactor with a quartz glass window. During the photocatalytic NRR experiment, 30 mg catalyst was dispersed in 120 mL ultrapure water. The reaction was carried out in a cell equipped with water circulation using a 300 W Xe lamp as the light source. The light source was positioned at a distance of 10 cm to the quartz reactor, whose intensity was 300 mW cm^{-2}, as measured using a visible-light radiometer. The mixture was continuously stirred in the dark and purified N$_2$ (purity ≥99.9%). Then, the light source was used to conduct photocatalytic NRR. During light irradiation, an aliquot (4 mL) of the dispersion was taken out of the photocatalytic reactor at set intervals (0 h, 1 h, 2 h, 3 h, 4 h, and 5 h) for NH$_4^+$ analysis. The concentration of NH$_4^+$ produced was quantified through the colorimetric method using Nessler's reagent (detected by absorbance at 420 nm) on a UV 2600 UV-vis spectrometer (Shimadzu, Japan). In a typical procedure, the aliquot was separated by centrifugation at 10 000 rpm for 15 min and transferred into a 3 mL colorimeter tube. Then, 100 μL of the potassium sodium tartrate solution was added to the sample tube. After adequate blending, 100 μL of Nessler's reagent was added to the sample tube and mixed for 10 min for ageing. Then, the UV absorption was measured by a UV 2600 spectrometer. The photocatalytic NRR sample was analyzed three times during all the measurements.

2.5 ^{1}H NMR spectra analysis

The isotope labelling experiments were carried out with 20 mg Zn/PbO/PC-Zn/MAPbBr$_3$ photocatalyst under ^{15}N$_2$ atmosphere. Then, 40.0 mL of the suspension was taken out from the photocatalytic reactor and separated by centrifugation at 10 000 rpm. The diluted 0.05 M HCl was concentrated to

4.0 mL by the reduced pressure distillation method to remove the solvent. D_2O/electrolyte mixed solution with a V_{D_2O} to $V_{electrolyte}$ ratio of 1 : 2 for ^1H NMR measurements was employed by the superconducting Fourier transform nuclear magnetic resonance spectrometer (Bruker Avance-400). The result is illustrated in Fig. 4c.

2.6 First-principles calculations

All spin-polarized DFT calculations were performed by the Vienna *Ab Initio* Simulation Package (VASP, version 5.4.4) with dispersion correction (DFT + D3). The interaction among the core electrons and valence electrons was implemented through the projected augmented-wave (PAW) method, and the energy cutoff was set to 450 eV for the plane-wave basis sets. The Perdew–Burke–Ernzerhof (PBE) functional within the generalized gradient approximation (GGA) was employed to describe the electronic exchange correlation interaction. It was well known that standard DFT was not good at dealing with strongly correlated systems containing d electrons, which would lead to an error. An intra-site Coulomb repulsion *U*-term was introduced to solve this problem, *i.e.*, the Hubbard *U* model, U_{eff} = 7.5 eV, was applied for Pt 5d electrons throughout the study.

To evaluate the computational capabilities and the impurity concentration obtained from the experiments, a model containing 192 atoms was established (95 Pb atoms, 1 Zn atom, and 96 O atoms for the Zn doped model; 94 Pb atoms, 1 Zn atom, 1 Pt atom, and 96 O atoms for Zn/Pt co-doped model). Except for 64 atoms in the bottom layer, all atoms of the slab models were allowed to relax in the process of structural optimization. The vacuum layer of all the slab models was set to 15 Å to avoid the interaction between the atoms in adjacent units perpendicular to the surface. A gamma-centered 1 × 1 × 1 *k*-point grid was set in the Brillouin zone, while the *k*-point grid was set to 3 × 3 × 1 for DOS calculation. The adsorption energies (E_{ad}) of N_2 or H atom were calculated using the following equations.

$$E_{ad} = E_{total} - E_{surface} - E_{N_2/H} \qquad (2)$$

where E_{total}, $E_{surface}$, and $E_{N_2/H}$ are the energy of adsorption configuration, (110) surface of the Zn doped model or Zn/Pt co-doped model, and N_2 or H, respectively.

The free energies of the species were calculated as:

$$\Delta G = \Delta E + \Delta ZPE - T\Delta S \qquad (3)$$

where ΔE is the reaction energy of the reactant and product molecules; the zero point energy (ΔZPE) and entropy (ΔS) were obtained from the calculation of vibration frequencies for the adsorbed species.

2.7 The ESI-based microdroplet synthesis

In the typical ESI-based microdroplet synthesis, physical and chemical processes were involved sequentially or simul-

taneously. For the cone-jet mode, the size of the droplets is usually determined by the following equation.

$$d = \alpha \frac{Q^a \varepsilon_0{}^b \rho^c}{\sigma^d \gamma^e} \qquad (4)$$

where d is the droplet diameter, α is a constant determined by the permittivity of the liquid, Q is the liquid volume flow rate, ε_0 is the permittivity of the free space, ρ is the mass density of the liquid, σ is the liquid conductivity, and γ is the surface tension of the liquid. The exponents a, b, c, d, and e in eqn (4) are constants.

The normalized time-resolved PL decay plots can be mathematically expressed by a bi-exponential equation.

$$\text{Fit} = A + B_1 \exp(-t/\tau_1) + B_2 \exp(-t/\tau_2) \qquad (5)$$

where τ_1 and τ_2 are the lifetime constants corresponding to radiative (fast) and nonradiative (slow) recombination components. A, B_1, and B_2 are constants obtained after fitting their decay curves. The average PL lifetime (τ_{avg}) can be calculated using the following equation.

$$\tau_{avg} = \frac{B_2\tau_2{}^2 + B_1\tau_1{}^2}{B_2\tau_2 + B_1\tau_1} \qquad (6)$$

τ_{avg} reflects the overall emission decay behavior of PbO/PC-MAPbBr$_3$, Zn/PbO/PC-Zn/MAPbBr$_3$, and Pt^{IV}/Zn/PbO/PC-Zn/MAPbBr$_3$.

3. Results and discussion

3.1 Preparation of PC-part-encapsulated Zn,Pt^{IV}-co-doped PbO-MAPbBr$_3$ heterojunction

The PC-part-encapsulated Zn,Pt-codoped PbO-MAPbBr$_3$ heterojunction of Pt^{IV}/Zn/PbO/PC-Zn/MAPbBr$_3$ was prepared by a one-step ESI-based microdroplet synthesis in microseconds.[32] In brief, a DMF solution containing MABr, PC, PbBr$_2$, H$_2$PtCl$_6$, and C$_4$H$_8$O$_4$Zn were fed into ESI flow. As illustrated (Scheme 1), under supersonic N$_2$ flow (160 L min^{-1}) and a DC voltage (+20 kV), ESI was employed to generate reactors of charged microdroplets. With rapid solvent evaporation in the accelerated gas (N$_2$ and O$_2$), the reactants were highly reactive to accelerate both Pt^{IV}/Zn/MAPbBr$_3$ crystallization and PC encapsulation. In this rapid synthesis, surface Zn was active for the substitution of internal Pb to obtain Zn/PbO/PC-Zn/MAPbBr$_3$ heterojunction. Simultaneously, the heterojunction was further co-doped by Pt^{IV}, which formed the Type I heterojunction (Pt^{IV}/Zn/PbO/PC-Zn/MAPbBr$_3$) to enhance the NRR.

3.2 Morphology characterizations

Morphology characterizations were employed to evaluate the synthesis of the Pt^{IV}/Zn/PbO/PC-Zn/MAPbBr$_3$ heterojunction. Three nanomaterials, including PbO/PC-MAPbBr$_3$ without any surface doping, single Zn-doped Zn/PbO/PC-Zn/MAPbBr$_3$, and the present Pt^{IV}/Zn co-doped one were prepared for the comparison. As demonstrated by transmission electron microscopy (TEM) images in Fig. 1a–c, three nanomaterials were well dis-
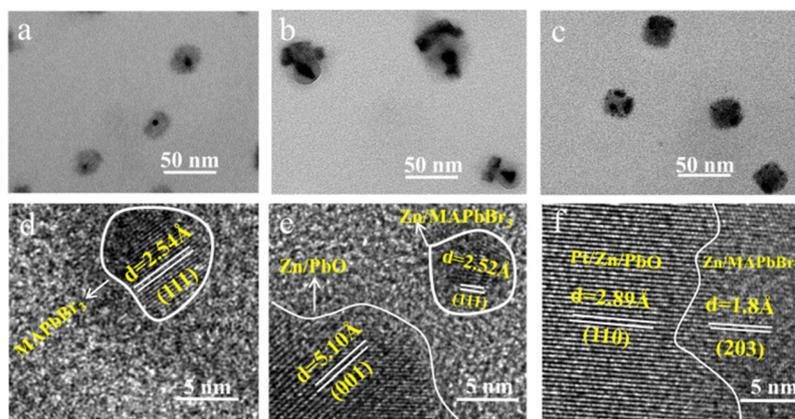
Fig. 1 Morphological characterization. TEM images of (a) PbO/PC-MAPbBr$_3$, (b) Zn/PbO/PC-Zn/MAPbBr$_3$ and (c) Pt^{IV}/Zn/PbO/PC-Zn/MAPbBr$_3$. HRTEM images of (d) PbO/PC-MAPbBr$_3$, (e) Zn/PbO/PC-Zn/MAPbBr$_3$ and (f) Pt^{IV}/Zn/PbO/PC-Zn/MAPbBr$_3$.

persed. The particle diameters varied from 20–25 nm for non-doped PbO/PC-MAPbBr$_3$ to 60–80 nm for single Zn-doped Zn/PbO/PC-Zn/MAPbBr$_3$, and to 40–45 nm for Pt^{IV}/Zn/PbO/PC-Zn/MAPbBr$_3$. This could be generated from their difference in the liquid conductivity of ESI.[62]

In more detail, successfully obtaining the PC-part-encapsulated Zn,Pt-codoped PbO-MAPbBr$_3$ heterojunction was confirmed by multiple characterizations. As demonstrated by high-resolution transmission electron microscopy (HRTEM), only significant (111) planes of MAPbBr$_3$ with a spacing of 2.5 Å were recorded (Fig. 1d) for PbO/PC-MAPbBr$_3$, while the (001) plane of Zn/PbO (5 Å spacing) and (110) plane of Pt/Zn/PbO (2.9 Å spacing) were recorded for single Zn-doped and Pt^{IV}/Zn-codoped ones, respectively (Fig. 1e and f). Compared to the non-doped materials (Fig. 1a), more PbO were exposed on two doped surfaces (Fig. 1b and c, Fig. S1†). This PC-part-encapsulated structures, by doping with Zn or Pt^{IV}/Zn, were further confirmed by high-angle annular dark field-scanning transmission electron microscopy (HAADF-STEM) (Fig. S2 and S3†). This exposure of PbO or doped-PbO was essential for heterojunction construction, which promoted charge transfer to boost the photocatalytic NRR. Moreover, as confirmed by EDX line scanning from HAADF-STEM (Fig. S4 and S5†), ~10 nm of internal Zn/MAPbBr$_3$ OIP QDs connected with the surface Zn/PbO or Pt^{IV}/Zn/PbO to form the heterojunction. Therefore, OIP QDs cores were partly encapsulated by PC, whose surfaces were confirmed to be doped with the exposed species of Zn/PbO or Pt^{IV}/Zn/PbO.
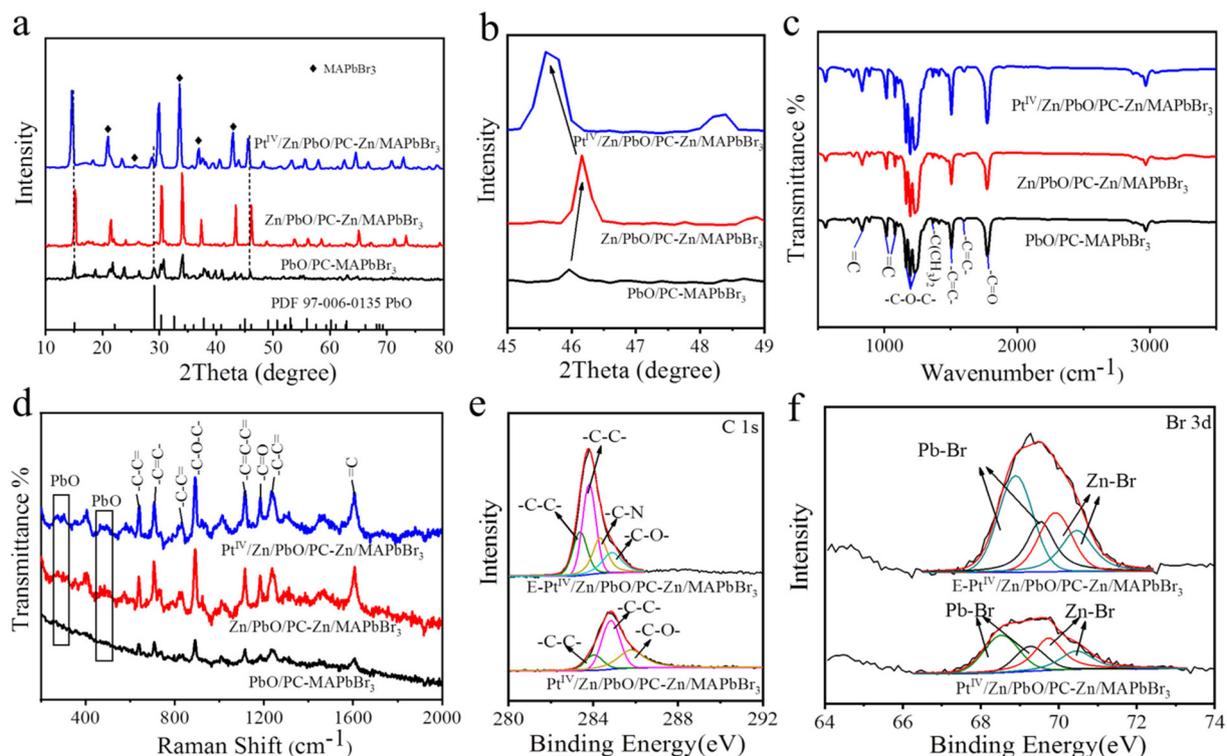
3.3 Chemical characterization

The crystal and chemical properties of the three OIP QDs were further examined. As demonstrated in the X-ray diffraction (XRD), the characteristic peaks of cubic MAPbBr$_3$ and PbO were recorded in the XRD patterns of the three materials (labelled in Fig. 2a). Compared with the non-doped one, the XRD peaks of PbO slightly shifted toward a higher angle when doped with Zn (red line, Fig. 2b), while a shift toward a lower angle was recorded after co-doping with Pt^{IV}/Zn (blue line,

Fig. 2b). These shifts indirectly confirmed the successful doping with Zn or Pt^{IV}/Zn due to the changing PbO interplanar spacing.[63] Furthermore, the successful encapsulation of OIP QDs by PC was demonstrated by Fourier Transform infrared (FTIR) (Fig. 2c) and Raman spectroscopy (Fig. 2d). The assignments of FTIR and Raman peaks for PC are summarized in Tables S1 and S2,† respectively.

Besides, the PC encapsulation of OIP QDs in three materials was also confirmed by the X-ray photoelectron spectra (XPS) of C 1s (Fig. 2e, Fig. S6c†). The –C–N characteristic peaks were recorded after etching, which belonged to the main component of MA in the Zn/MAPbBr$_3$ core. The corresponding PC peaks were also observed (summarized in Table S3†). Furthermore, the higher Pb–Br signals were interiorly exhibited in Pt^{IV}/Zn/PbO/PC-Zn/MAPbBr$_3$ (Fig. 2f), also generated from the core components of Zn/MAPbBr$_3$. These observations were in accordance with the PC-encapsulated structure of Zn/MAPbBr$_3$ OIP QDs. Besides, the Pb–O Raman peaks increased after doping corresponding to the link region of Pb–O in the ending mode (Fig. 2d). This demonstrated that the content of exposed PbO on the surface increased after doping. Therefore, the OIP QDs were confirmed to be part-encapsulated by PC with PbO exposed on the surface, which was beneficial for guaranteeing the NRR in aqueous solutions.

Moreover, the doping details were examined by the comparison of XPS signals on the surface and inside Pt^{IV}/Zn/PbO/PC-Zn/MAPbBr$_3$. To characterize the inside components, the materials were etched by Ar ion. Without etching, the significant peaks of Pb–O (on Pb 4f spectra, Fig. 3a), Zn–O (on Zn 2p spectra, Fig. 3b), and Pt–O (on Pt^{IV} 4f spectra, Fig. 3c) were observed on the surface of Pt^{IV}/Zn/PbO/PC-Zn/MAPbBr$_3$. This was in accordance with the surface co-doping by Pt^{IV}/Zn. After etching, the interior signals of Pb–Br and Zn–Br are higher than those of Pb–O and Zn–O (Fig. 3a and b), which indicated that Zn/MAPbBr$_3$ PQDs were the main core components. In addition, Pt was mainly distributed on the surface of Pt^{IV}/Zn/PbO/PC-Zn/MAPbBr$_3$ because no significant interior Pt^{IV} signal was observed after etching (Fig. 3c). Except for the aforemen-

Fig. 2 Chemical characterization of PbO/PC-MAPbBr$_3$, Zn/PbO/PC-Zn/MAPbBr$_3$ and Pt^{IV}/Zn/PbO/PC-Zn/MAPbBr$_3$. (a) XRD patterns. Dotted lines are the sectional PbO characteristic patterns. (c) FTIR spectra. (d) Raman spectra. XPS spectra of C 1s (e) and Br 3d (f) for Pt^{IV}/Zn/PbO/PC-Zn/MAPbBr$_3$ with and without etching.
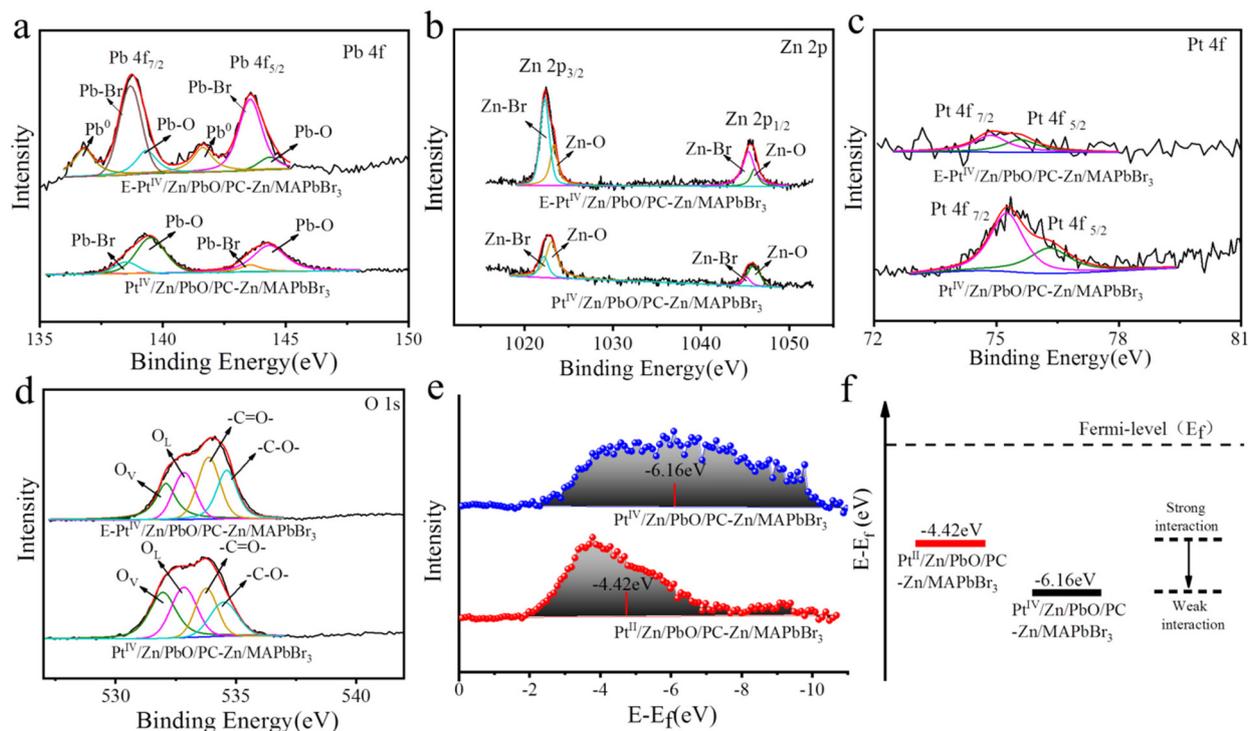
Fig. 3 XPS spectra of Pb 4f (a), Zn 2p (b), Pt 4f (c), and O 1s (d) of non-etched and 20 nm-etched Pt^{IV}/Zn/PbO/PC-Zn/MAPbBr$_3$. (e) The d-band center of Pt^{II}/Zn/PbO/PC-Zn/MAPbBr$_3$ and Pt^{IV}/Zn/PbO/PC-Zn/MAPbBr$_3$. (f) Schematic illustrating the shift of the d-band away from the Fermi level to weaken the metal–H interaction. The red and black lines represent their d-band centers.

tioned species observed on the surface, the C 1s peaks of PC (Fig. 2e, Table S3†) were also recorded, demonstrating the part-encapsulation by PC. This guaranteed the good water-resistance of $Pt^{IV}/Zn/PbO/PC-Zn/MAPbBr_3$ for NRR in aqueous conditions.

Furthermore, the doping by Zn species promoted the substitution of Pb by Zn atoms to expose PbO on the surface. This was demonstrated by the comparsion of surface PbO between $PbO/PC-MAPbBr_3$ and $Zn/PbO/PC-Zn/MAPbBr_3$ (Fig. S6†), which was beneficial for further Pt^{IV}/Zn co-doping to obtain the heterojunction with active sites. Moreover, the O 1s XPS spectra (Fig. 3d) indicated the presence of Pb–O lattice oxygen (OL) and oxygen vacancy (OVs) on the $Pt^{IV}/Zn/PbO/PC-Zn/MAPbBr_3$ surface, in addition to $–C=O–$ and $–C–O–$ species of PC (at 533.85 eV and 538.51 eV of BE). The C 1s peaks of PC (Fig. S6c, Table S3†) also confirmed the PC encapsulation. Therefore, the co-doped $Pt^{IV}/Zn/PbO$ was on the PC-part-encapsulated $Pt^{IV}/Zn/PbO/PC-Zn/MAPbBr_3$, which constructed a core–shell-like heterojunction to improve photocatalytic NRR in aqueous solutions.

As we know, the d-band center is related to the adsorption between the catalysts and adsorbates, which can be used to predict the catalytic reactivities.[54,64] Therefore, the d-band states of the Pt^{IV} for Pt–H interaction were examined to predict the competition reaction between NRR and HER. As shown in Fig. 3c, the wide XPS peaks on the Pt 4f spectra were deconvoluted into two peaks of Pt^{IV} oxide states (75.3 eV and 76.3 eV), which indicated the decreased Pt electron density on the surface. For comparison, the Pt^{II}-doped nanomaterials of $Pt^{II}/Zn/PbO/PC-Zn/MAPbBr_3$ were prepared using K_2PtCl_4 as the Pt^{II} source. As shown in Fig. S7,† two wide peaks of Pt^{II} oxide states (at ~75.5 eV and ~72 eV) were recorded. Thereafter, the d-band states of both Pt^{IV} and Pt^{II}-doped nanomaterials were calculated based on their corresponding XPS data. As shown in Fig. 3e, the initial d-band center of $Pt^{IV}/Zn/PbO/PC-Zn/MAPbBr_3$ (−6.16 eV) was much lower than that of $Pt^{II}/Zn/PbO/PC-Zn/MAPbBr_3$ (−4.42 eV). This resulted in the weaker Pt–H interaction in $Pt^{IV}/Zn/PbO/PC-Zn/MAPbBr_3$ than in $Pt^{II}/Zn/PbO/PC-Zn/MAPbBr_3$, which exhibited a lower d-band state far away from its Fermi level (Fig. 3f). Hence, Pt d-orbitals were tuned by Pt^{IV}/Zn co-doped PbO on the surface, resulting a low d-band center far away from the Fermi level. Thus, the Pt–H interaction was weakened to suppress the HER, which resulted in increased NRR selectivity.

3.4 Evaluation on the NRR performance

The performance of photocatalytic NRR catalyzed by the $Pt^{IV}/Zn/PbO/PC-Zn/MAPbBr_3$ nanomaterials was examined using Ar or N_2 as the feed gas. Fig. 4a shows the NH_3 yields *versus* the irradiation times (10 h) for the materials $PbO/PC-MAPbBr_3$, $Zn/PbO/PC-Zn/MAPbBr_3$, and $Pt^{IV}/Zn/PbO/PC-Zn/MAPbBr_3$. Fed by N_2, only significant NH_3 was generated on catalysis by the doped nanomaterials of $Zn/PbO/PC-Zn/MAPbBr_3$ and $Pt^{IV}/Zn/PbO/PC-Zn/MAPbBr_3$. The comparison of the NH_3 yields
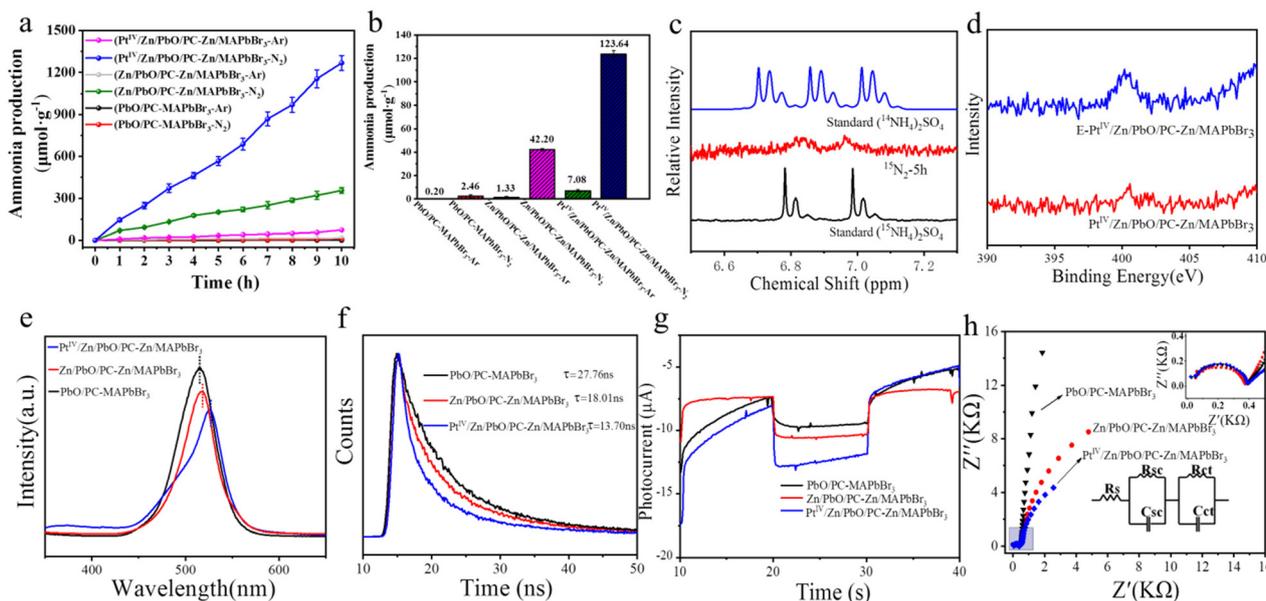
Fig. 4 Evaluation of the photocatalytic NRR catalyzed by $PbO/PC-MAPbBr_3$, $Zn/PbO/PC-Zn/MAPbBr_3$ and $Pt^{IV}/Zn/PbO/PC-Zn/MAPbBr_3$. (a) NH_3 yield *versus* irradiation time with N_2 and Ar as feed gases. (b) Average NH_3 yields. (c) ^1H NMR spectra of the NRR system with $^{15}N_2$ (99%) as the feed gas. Standards: $^{14}NH_4SO_4$ and $^{15}NH_4SO_4$. (d) N 1s XPS spectra of $Pt^{IV}/Zn/PbO/PC-Zn/MAPbBr_3$ and $E-Pt^{IV}/Zn/PbO/PC-Zn/MAPbBr_3$. (e) PL spectra, (f) TRPD spectra (excited at 280 nm), and (g) transient photocurrent responses of $PbO/PC-MAPbBr_3$, $Zn/PbO/PC-Zn/MAPbBr_3$ and $Pt^{IV}/Zn/PbO/PC-Zn/MAPbBr_3$. Conditions: +0.5 V *vs.* Ag/AgCl at pH 6.4 under chopped illumination with a fixed time interval. (h) Impedance curves for the materials before the stability test under 1.5 G illumination. Insets: Enlarged view of the blue area; equivalent circuit to fit the impedance data. R_S: The series resistance (including materials resistance and contact resistance of the system). R_{SC}: Charge transfer resistance at the electrode interface. R_{ct}: Charge transfer resistance at the electrolyte interface.

obtained by different catalysts are shown in Fig. 4b. The NH_3 yield catalyzed by $Pt^{IV}/Zn/PbO/PC-Zn/MAPbBr_3$ (116.56 μmol g_{cat}^{-1} h^{-1}) was higher than $Zn/PbO/PC-Zn/MAPbBr_3$ (40.87 μmol g_{cat}^{-1} h^{-1}), which exhibited an approximate linear increase with time (Fig. 4a). It should be noted that the present $Pt^{IV}/Zn/PbO/PC-Zn/MAPbBr_3$ exhibited a much higher NRR efficiency than the Pt-loaded nanoparticles ($Pt-Pt^{IV}/Zn/PbO/PC-Zn/MAPbBr_3$) (Fig. S9†), which could be caused by the stronger interaction between the loaded catalysts and H proton. Using Ar as the feed gas, trace NH_3 was also recorded by $Pt^{IV}/Zn/PbO/PC-Zn/MAPbBr_3$, which could be generated from the trace N element on the surface. In addition, the Pt^{II}/Zn co-doped catalyst exhibited a much lower NH_3 yield of 18.39 μmol g_{cat}^{-1} h^{-1} (Fig. S8†) due to the poor suppression of NRR to HER (demonstrated in Fig. 3f). Moreover, $Pt^{IV}/Zn/PbO/PC-Zn/MAPbBr_3$ was stable enough for the NRR reaction, even retaining about 95% of the orignial intensity in aqueous solutions at the 10th day (Fig. S10†). Therefore, the present materials were demonstrated to be water resistant and possessed good stability in aqueous solutions after the NRR reaction, which is attributed to the PC-encapsulation to protect perovskite QDs.

To further confirm N_2 fixation *via* photocatalytic NRR catalyzed by $Pt^{IV}/Zn/PbO/PC-Zn/MAPbBr_3$, an isotope-labelling experiment was employed using $^{15}N_2$ (99%) as the feed gas. NRR was employed in 120 mL H_2O containing 30 mg catalyst, and the production was characterized by ^1H NMR measurements. As shown in Fig. 4c, two peaks of $^{15}NH_4^+$ (at 6.88 and 6.96 ppm) were observed after 5 h, confirming the N_2 fixation *via* NRR. Nevertheless, the trace N (Fig. 4d) on the surface could also contribute to the generation of a small amount of NH_3 at the beginning.

The comparison of the photoluminescence (PL) responses of the three materials was further employed to examine the Pt^{IV}/Zn co-doped performance. The steady-state PL spectra in Fig. 4e exhibits the relatively weak and red-shift emission with Pt^{IV}/Zn co-doped. This indicated a suppressed irradiative recombination of the photoexcited electron-holes in $Pt^{IV}/Zn/PbO/PC-Zn/MAPbBr_3$, which resulted in the fast transfer of internal photogenerated electron-holes to the shell. Furthermore, the faster charge transfer was also confirmed by the decay traces of the time-resolved photoluminescence decay (TRPD) spectra. Excited at 280 nm, the decay traces were fitted using biexponential decay kinetics with low uncertainties (χ) (Table S4†). As shown in Fig. 4f, the $Pt^{IV}/Zn/PbO/PC-Zn/MAPbBr_3$ composite ($\tau_{average} = 13.70$ ns) decayed distinctly faster than $Zn/PbO/PC-Zn/MAPbBr_3$ ($\tau_{average} = 18.01$ ns) and $PbO/PC-MAPbBr_3$ ($\tau_{average} = 27.76$ ns). Therefore, the decreased $\tau_{average}$ confirmed the rapid charge transfer between the $Zn/MAPbBr_3$ core and the $Pt^{IV}/Zn/PbO$ shell in a facile nonradiative quenching channel.[24] This could be attributed to more exposed electron-withdrawing active sites of Pt^{IV}.[57]

Subsequently, the photoelectrochemical (PEC) performances of the three catalysts were evaluated by photocurrent and electrochemical impedance examinations in N_2 conditions. As shown in Fig. 4g, the highest transient photo-current responses by $Pt^{IV}/Zn/PbO/PC-Zn/MAPbBr_3$ were recorded with an interval chopped illumination. This indicated a more efficient separation of photogenerated electron-hole by the co-doped Pt^{IV}/Zn catalyst.[41] This was attributed to the formation of the improved Type I heterojunction with the Pt^{IV} active sites exposed on the surface of $Pt^{IV}/Zn/PbO/PC-Zn/MAPbBr_3$. The consistent charge-transfer properties by the heterojunction were further examined by electrochemical impedance spectroscopy tests. As a result, the R_{SC} and R_{CT} of $Pt^{IV}/Zn/PbO/PC-Zn/MAPbBr_3$ were the lowest under AM 1.5 G illumination (Fig. 4h, the fitting data are list in Table S5†) and showed good stability even after the NRR stability test (Fig. S11,† the fitting data are list in Table S6†). This demonstrated that the Pt^{IV}/Zn co-doped nanomaterials facilitated the charge transfer and promoted electron delocalization at the interface between the heterojunction and the semiconductor/electrolyte. Therefore, codoped with the electron-deficient sites of Pt^{IV}, the d-band center was lowered to improve the heterojunction. This would increase the N_2 adsorption on the Pt^{IV} active sites, therefore enhancing charge transfer and separation to benefit NRR.

3.5 The band structures of $Pt^{IV}/Zn/PbO/PC-Zn/MAPbBr_3$

To understand the dynamics of light absorption as well as the charge separation and charge transfer during NRR, the band structure of $Pt^{IV}/Zn/PbO/PC-Zn/MAPbBr_3$ was investigated. Firstly, the Tauc plots of the $Pt^{IV}/Zn/PbO$ shell and the $Zn/MAPbBr_3$ core were obtained based on UV-vis absorption spectroscopy. As shown in Fig. 5a, the calculated energy band gaps were 3.3 and 3.6 eV for $Pt^{IV}/Zn/PbO$ and $Zn/MAPbBr_3$, respectively. Deduced by the secondary-electron emission (SEE) spectra recorded by an ultraviolet photoelectron spectrophotometer (UPS), the work functions of $Pt^{IV}/Zn/PbO$ and $Zn/MAPbBr_3$ were plotted (Fig. 5b). The valence band X-ray photoelectron spectra (VBXPS) revealed the energy difference between the Fermi level and the valence-band maximum ($E_F - E_V$). As demonstrated in Fig. 5c, the energy differences were 2.38 and 2.48 eV for $Pt^{IV}/Zn/PbO$ and $Zn/MAPbBr_3$, respectively. The schematic energy band diagrams of $Pt^{IV}/Zn/PbO$ and $Zn/MAPbBr_3$ are shown in Fig. 5d, indicating an efficient Type (I) heterojunction with Pt^{IV}/Zn co-doped on the surface.

3.6 The examination of the atomic dispersions of $Pt^{IV}/Zn/PbO/PC-Zn/MAPbBr_3$

The atomic dispersions of Pb, Zn, and Pt^{IV} as well as their coordination environments were further examined by X-ray absorption near-edge structures (XANES) and extended X-ray absorption fine structure (EXAFS) measurements (Fig. S12†). As shown in Fig. 6a, the metallic signals of Pb–O at about 2.163 Å was recorded on the surface of $Pt^{IV}/Zn/PbO/PC-Zn/MAPbBr_3$. This manifested that the PbO was exposed on the surface of PC-encapsulated OIP QDs to guarantee the charge transport in NRR. In addition, the Fourier transformation (FT) of the Zn K-edge spectra was conducted with Zn foil, $ZnBr_2$, and ZnO as references. As demonstrated (Fig. 6b), the typical Zn–O scattering paths of $Zn/PbO/PC-Zn/MAPbBr_3$ and $Pt^{IV}/Zn/$
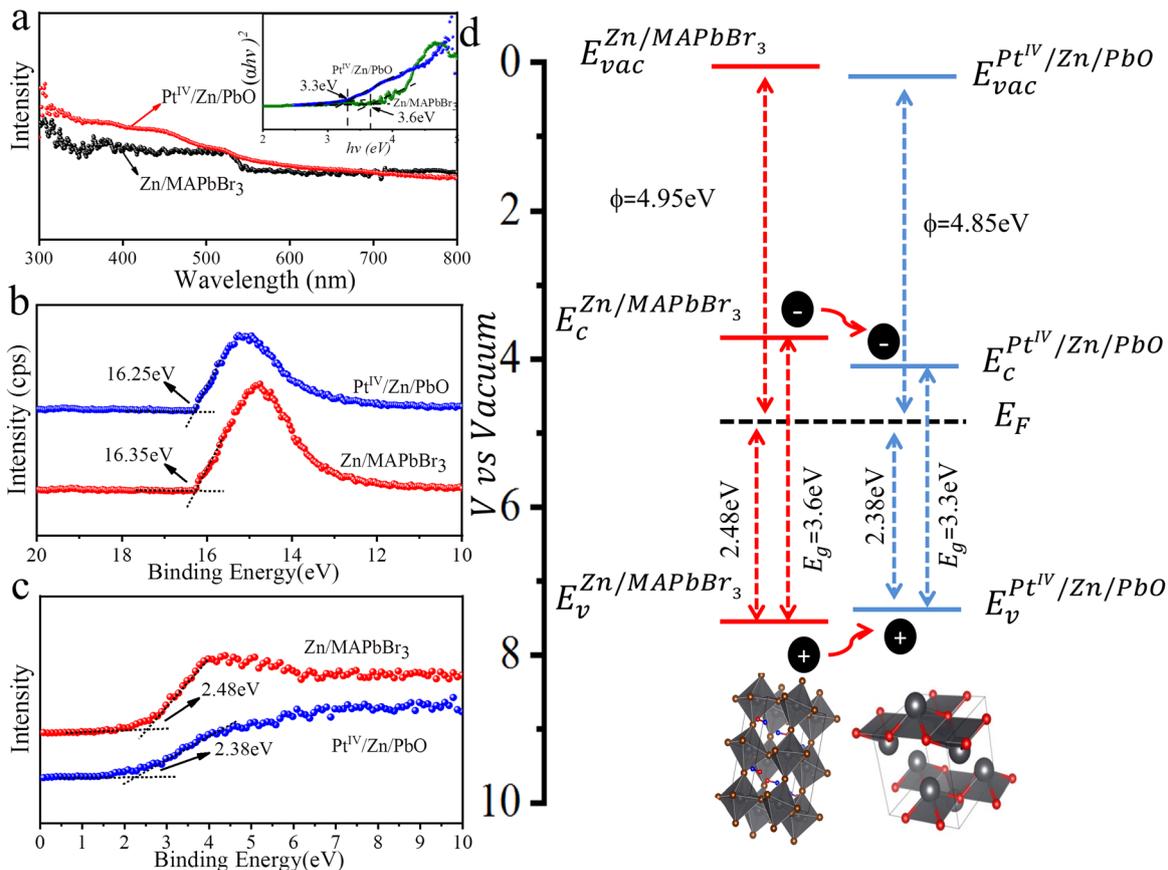
Fig. 5 Band structures of $Pt^{IV}/Zn/PbO/PC-Zn/MAPbBr_3$. (a) The calculations of the optical band gap. (b) UPS spectra. (c) VBXPS spectra. (d) Schematic energy band diagram of the $Pt^{IV}/Zn/PbO/PC-Zn/MAPbBr_3$ heterojunction.
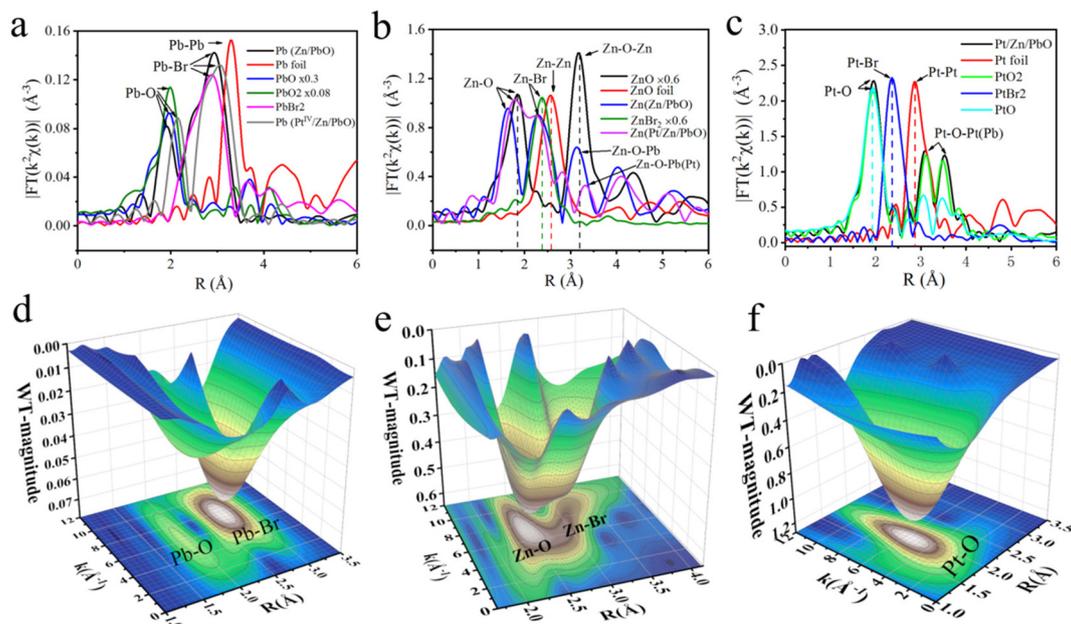

Fig. 6 FT K^2-weighted XANES spectra of (a) Pb and (b) Zn and the (c) Pt^{IV} K-edge radial distance spectra $\chi(R)$ for three OIP QDs, as well as the references of Pb foil, PbO, PbO_2, $PbBr_2$, Zn foil, $ZnBr_2$, ZnO, Pt foil, PtO_2, $PtBr_2$ and PtO at the K-edge. Wavelet transform extended X-ray absorption fine structure (WTEXAFS) of $Pt^{IV}/Zn/PbO/PC-Zn/MAPbBr_3$ for (d) Pb, (e) Zn and (f) Pt^{IV}.

PbO/PC-Zn/MAPbBr$_3$ at about 1.802 Å and 1.809 Å, respectively, were recorded on the surface, while the signals of Zn–Br (at 2.310 Å and 2.220 Å) were observed for the Zn-doped and Pt^{IV}/Zn co-doped nanomaterials.

Moreover, the FT K^2-weighted XANES spectrum of Pt in Pt^{IV}/Zn/PbO/PC-Zn/MAPbBr$_3$ was also recorded. As shown in Fig. 6c, with PtO$_2$ (5d^6) as the reference, the Pt–O coordination at about 1.993 Å was recorded. This indicated a high valence state of ~4+ with a larger population of unoccupied Pt 5d states in the Pt^{IV}/Zn co-doped OIP QDs. Thus, the electron-deficient catalytic sites with strong affinity toward N$_2$ were formed. Compared with the FT K^2-weighted XANES spectra of Pb (Fig. 6a) and Zn (Fig. 6b), this dispersion of Pt and Zn on the surface could be generated from the substation of Pb species by Zn and Pt on the surface. Furthermore, there were no Pt–Pt and Pt–Br peaks on the surface of Pt^{IV}/Zn/PbO/PC-Zn/MAPbBr$_3$ (Fig. 6c), suggesting that only the atomically dispersed Pt element existed on the surface. The recorded electron deficient sites of Pt^{IV} and Zn together with the Pb–O signals on the surface are in accordance with the XPS observations.

To better demonstrate the dispersed state of Pb, Zn, and Pt in Pt^{IV}/Zn/PbO/PC-Zn/MAPbBr$_3$, the wavelet transform (WT) of $\chi(R)$ was employed compared with the corresponding references (Pb foil, PbO, PbO$_2$, PbBr$_2$, Zn, ZnBr$_2$, ZnO, Pt foil, PtO$_2$, PtBr$_2$, and PtO in Fig. S14–S16†). In the wavelet transform extended X-ray absorption fine structure (WTEXAFS) of Pb (Fig. 6d), the significant signals of Pb–O and Pb–Br were observed on the surface of the Pt^{IV}/Zn co-doped nanomaterials. This confirmed the exposure of PbO on the surface to construct the heterojunction for NRR. As demonstrated in Fig. 6e, the scattering path signal of Zn–O bonding at [$\chi(k)$, $\chi(R)$] of [7.012, 1.809] was recorded on the surface, which was under the internal Zn–Br signal (at [$\chi(k)$, $\chi(R)$] of [6.502, 2.221]). This demonstrated the successful doping of Zn to form a coordination shell on the surface. More interestingly, compared with the reference signal of Pt–Pt in Pt foil at [7.493,

2.850] (Fig. S14†), no Pt–Pt bonding was observed in Pt^{IV}/Zn/PbO/PC-Zn/MAPbBr$_3$, while only a significant Pt–O signal at [$\chi(k)$, $\chi(R)$] of [5.812, 1.990] was recorded on the surface (Fig. 6f), and no other scattering path signal of Pt was observed. This indicated the atomically dispersed state of Pt^{IV} atoms on the Pt^{IV}/Zn/PbO/PC-Zn/MAPbBr$_3$ nanomaterials, which lowered the d-band to weaken H adsorption. The formation of an Zn/PbO oxide shell might be due to the oxidation of the nanostructure in air. Quantitative $\chi(R)$ space spectra fitting was also performed to investigate the local atomic structure for determining the coordination numbers of Pb, Zn, or Pt on the surface (Tables S7–S9†). Br was mainly in the core structure, which was one of the main components of OIP QDs. Therefore, the significant signals of the co-doped species of Pt^{IV} and Zn confirmed to be connected to PbO exposed on the surface.

3.7 Mechanism studies by theoretical calculations

To further explore the roles of Pt/Zn co-doped atoms on the surface of Pt/Zn/PbO/PC-Zn/MAPbBr$_3$ for photocatalytic NRR, first-principle theoretical calculations were employed. Herein, a series of DFT calculations were performed to examine the atomic structure of Zn-doped and Pt/Zn co-doped active sites. Fig. S17† shows the optimized models, in which the bond lengths are 1.868 Å and 2.142 Å for Zn–O and Pb–O, respectively. These lengths are in accordance with the structural parameters in the Zn and Pb K-edge $\chi(R)$ space spectral fitting of Pt^{IV}/Zn-PbO (Fig. 6). The N$_2$ molecule is able to be adsorbed on the catalyst surface either in side-on or end-on configurations. Based on the calculated adsorption energy and bond length (Fig. 7), the end-on configuration on the Pt^{IV}/Zn co-doped surface is the favorable one with an adsorption energy of −1.18 eV (Fig. 7(v)). This is obviously superior to the adsorption energy on the Zn-doped surface (−0.48 eV) (Fig. 7(ii)). By energy minimization, N$_2$ would eventually lean toward the Pt site after adsorbing on the surface either in end-on or side-on configuration. This demonstrated that Pt acted as the active
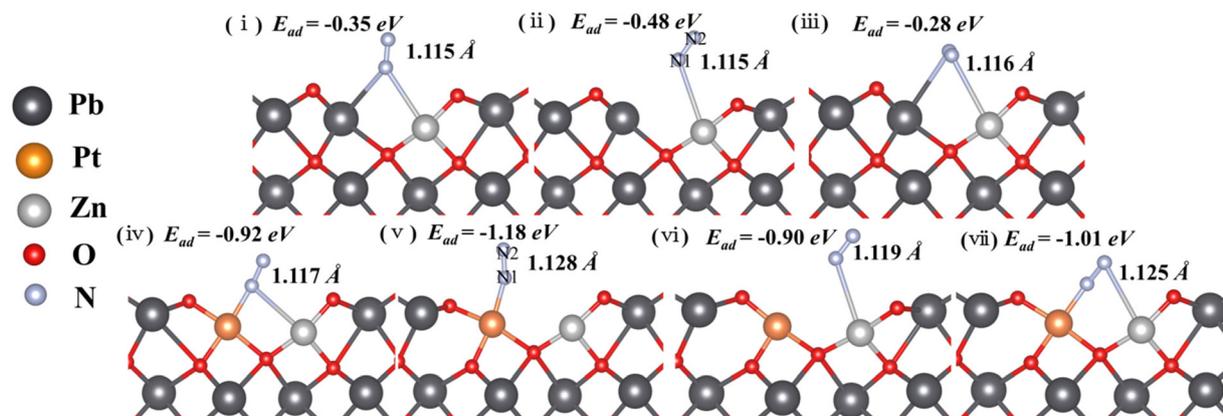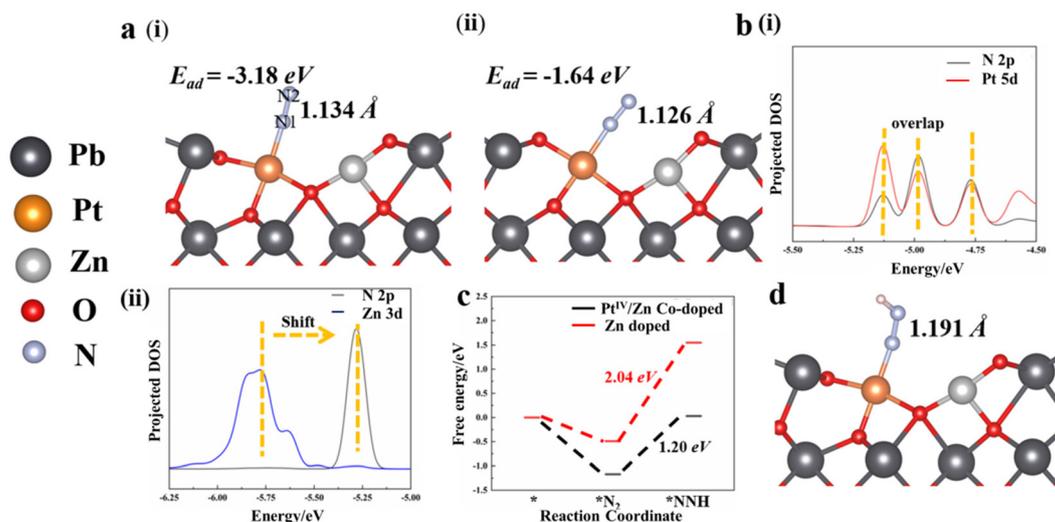

Fig. 7 Adsorption energy and the bond length of N$_2$ absorbed on the surface of Zn-doped (i, ii and iii) and Pt^{IV}/Zn co-doped (iv, v and vi) catalysts in both end-on and side-on configurations. The interactions between the oxygen vacancy and Pb, Pt and Zn were examined.

Fig. 8 (a) N$_2$ absorbed on the (i) Pt^{IV} site and oxygen vacancy in the Zn/Pt^{IV} co-doped model with (ii) side-on configuration in the charged system. (b) Projected DOS of the (i) Zn/Pt co-doped and (ii) Zn-doped model. (c) Free energy profiles of the formation of *NNH in the Zn-doped and Zn/Pt^{IV} co-doped systems. (d) The optimized structure of *NNH adsorbed on the Zn/Pt^{IV} co-doped system.

site for NRR. Therefore, the active sites of Pt on the catalyst surface were identified to enhance the adsorption of N$_2$ for NRR.

In addition, Bader charge analysis was performed to evaluate the polarization of N$_2$ by the catalysts. The charges on N1 and N2 of the Zn-doped catalyst model are +0.09e and −0.09e, respectively (Fig. 7(vi)), while in the Pt/Zn co-doped one, the charges on the two nitrogen atoms are +0.22e and −0.27e, respectively (Fig. 7(v)). This indicates that the doped Pt facilitates the polarization of N$_2$. The adsorption of N$_2$ on Pt^{IV} was further examined by removing two electrons from the aforementioned Pt–Zn co-doped system, which displayed a higher adsorption energy of −3.18 eV (Fig. 8a(i)). The N–N triple bond is correspondingly activated and extended to 1.134 Å between the length of triple bond (1.091 Å) of N$_2$ and the double bond (1.200 Å) of diazene. Meanwhile, in this charged system, in the end-on configuration, the polarization of N$_2$ is further enhanced with electronic charges of +0.33 and −0.23e on N1 and N2, respectively (Fig. 8a(i)). On the contrary, the adsorption of N$_2$ on Pt^{IV} in the side-on configuration is not stable, which is eventually converted into the adsorption to Pt^{IV} in the end-on configuration after energy minimization (Fig. 8a(ii)). Therefore, the end-on configurations with N$_2$ adsorbed on Pt^{IV} in the Pt^{IV}/Zn co-doped model as well as the Zn-doped one were adopted for the following calculations.

The suppression of NRR to HER by the Pt^{IV}/Zn co-doped catalysts was further examined by calculating the adsorption energies of H and N$_2$ on the surface. Significantly, in both neutral and charged systems, the H atom always tends to be adsorbed to the adjacent O atom, irrespective of its initial location (on top of Pt^{IV} or Zn, Fig. S18†). On the other hand, with stronger metal–N$_2$ interaction, Pt^{IV} is favored to adsorb N$_2$ over H to enhance the NRR activity because the Pt^{IV} d-band states were far from the Fermi level (E_f).[54] Thus, the active site

of Pt^{IV} tends to adsorb N$_2$, which suppresses HER to increase the NRR efficiency, indicating that water would not act as the electron acceptor.

To further investigate the origin of the catalytic activity of the Pt^{IV}/Zn co-doped system, the electronic properties of the contacting interface were examined. As demonstrated by the projected DOS, the Pt 5d and N 2p overlap significantly (Fig. 8b(i)), while a significant shift is observed between the DOS signals of Zn 3d and N 2p (Fig. 8b(ii)). This confirms the intensive electron transfer between Pt^{IV} and N, which plays a dominant role in the catalytic activity for NRR. Considering that the formation of *NNH was generally regarded as the rate-determining step of NRR, the reaction energy barrier of the proton-coupled electron transfer process (*N$_2$ + H$^+$ + e$^-$ → *NNH) was calculated. It was found that the reaction from *N$_2$ to *NNH requires an uphill free energy of 2.04 eV on Zn-doped and 1.20 eV on Pt^{IV}/Zn co-doped system, respectively (Fig. 8c). This results in a significantly elongated length of the N–N bond from 1.134 Å (in *N$_2$) to 1.191 Å (in *NNH) (Fig. 8d), indicating that N$_2$ tends to be dissociated at the *NNH state. In addition, the lower reaction energy barrier of the Pt^{IV} active site is also obtained to facilitate catalytic NRR.

4. Conclusion

In conclusion, by ESI-based preparation, the PC-part-encapsulated type I heterojunction of Pt^{IV}/Zn co-doped PbO-MAPbBr$_3$ was successfully constructed in microseconds. In this rapid process, the core of Zn/MAPbBr$_3$ was crystallized, followed by the encapsulation of the PC shell to obtain the water-resistant properties. Significantly, the synergistic co-doping structure of Pt^{IV}/Zn with exposed PbO was constructed on the surface. This facilitated the formation of active sites of electron-deficient

d-orbital of Pt atoms with strong affinity towards N_2 to suppress HER. Therefore, NRR was boosted by Pt^{IV}/Zn co-doped active sites with lower reaction energy barrier due to the improved electron delocalization of Pt^{IV} d-orbitals for electron transfer to N_2. The developed enhanced heterojunction of water-resistant Pt^{IV}/Zn co-doped OIP QDs has encouraged the applications of OIP QDs in the aqueous phase. Furthermore, this could also be helpful in more photocatalytic applications of green synthesis.

Conflicts of interest

The authors declare that they have no known competing financial interests or personal relationships that could have appeared to influence the work reported in this paper.

Acknowledgements

References

1 H. Huang, J. Raith, S. V. Kershaw, S. Kalytchuk, O. Tomanec, L. H. Jing, A. S. Susha, R. Zboril and A. L. Rogach, *Nat. Commun.*, 2017, **8**, 8.

2 M. M. Lee, J. Teuscher, T. Miyasaka, T. N. Murakami and H. J. Snaith, *Science*, 2012, **338**, 643–647.

3 Y. Cao, N. Wang, H. Tian, J. Guo, Y. Wei, H. Chen, Y. Miao, W. Zou, K. Pan, Y. He, H. Cao, Y. Ke, M. Xu, Y. Wang, M. Yang, K. Du, Z. Fu, D. Kong, D. Dai, Y. Jin, G. Li, H. Li, Q. Peng, J. Wang and W. Huang, *Nature*, 2018, **562**, 249–253.

4 N. Li, L. Song, Y. Jia, Y. Dong, F. Xie, L. Wang, S. Tao and N. Zhao, *Adv. Mater.*, 2020, **32**, 1907786.

5 C. Wang, G. Dai, J. Wang, M. Cui, Y. Yang, S. Yang, C. Qin, S. Chang, K. Wu, Y. Liu and H. Zhong, *Nano Lett.*, 2022, **22**, 1338–1344.

6 Q. Cui, X. Song, Y. Liu, Z. Xu, H. Ye, Z. Yang, K. Zhao and S. Liu, *Matter*, 2021, **4**, 2490–2507.

7 J. Zhao, L. Zhao, Y. Deng, X. Xiao, Z. Ni, S. Xu and J. Huang, *Nat. Photonics*, 2020, **14**, 612–617.

8 Y. X. Wang, R. X. Lin, P. C. Zhu, Q. H. Zheng, Q. J. Wang, D. Y. Li and J. Zhu, *Nano Lett.*, 2018, **18**, 2772–2779.

9 Y. Q. Wu, P. Wang, X. L. Zhu, Q. Q. Zhang, Z. Y. Wang, Y. Y. Liu, G. Z. Zou, Y. Dai, M. H. Whangbo and B. B. Huang, *Adv. Mater.*, 2018, **30**, 6.

10 X. Tian, S. D. Stranks and F. You, *Nat. Sustain.*, 2021, **4**, 821–829.

11 S. Tan, T. Huang, I. Yavuz, R. Wang, T. W. Yoon, M. Xu, Q. Xing, K. Park, D.-K. Lee, C.-H. Chen, R. Zheng, T. Yoon, Y. Zhao, H.-C. Wang, D. Meng, J. Xue, Y. J. Song, X. Pan, N.-G. Park, J.-W. Lee and Y. Yang, *Nature*, 2022, **605**, 268–273.

12 J. Zeng, L. Bi, Y. Cheng, B. Xu and A. K.-Y. Jen, *Nano Res. Energy*, 2022, e9120002.

13 J. H. Heo, S. H. Im, J. H. Noh, T. N. Mandal, C.-S. Lim, J. A. Chang, Y. H. Lee, H.-j. Kim, A. Sarkar, M. K. Nazeeruddin, M. Graetzel and S. I. Seok, *Nat. Photonics*, 2013, **7**, 487–492.

14 Y. Q. Wu, P. Wang, Z. H. Guan, J. X. Liu, Z. Y. Wang, Z. K. Zheng, S. Y. Jin, Y. Dai, M. H. Whangbo and B. B. Huang, *ACS Catal.*, 2018, **8**, 10349–10357.

15 F. Chen, C. X. Xu, Q. Y. Xu, Y. Z. Zhu, F. F. Qin, W. Zhang, Z. Zhu, W. Liu and Z. L. Shi, *ACS Appl. Mater. Interfaces*, 2018, **10**, 25763–25769.

16 L. Wang, H. Xiao, T. Cheng, Y. Li and W. A. Goddard III, *J. Am. Chem. Soc.*, 2018, **140**, 1994–1997.

17 B. Wenger, P. K. Nayak, X. M. Wen, S. V. Kesava, N. K. Noel and H. J. Snaith, *Nat. Commun.*, 2017, **8**, 10.

18 Y. Wu, P. Wang, Z. Guan, J. Liu, Z. Wang, Z. Zheng, S. Jin, Y. Dai, M.-H. Whangbo and B. Huang, *ACS Catal.*, 2018, **8**, 10349–10357.

19 L. Quyet Van, K. Hong, H. W. Jang and S. Y. Kim, *Adv. Electron. Mater.*, 2018, **4**, 1800335.

20 J. Shamsi, A. S. Urban, M. Imran, L. De Trizio and L. Manna, *Chem. Rev.*, 2019, **119**, 3296–3348.

21 C. Caddeo, M. I. Saba, S. Meloni, A. Filippetti and A. Mattoni, *ACS Nano*, 2017, **11**, 9183–9190.

22 S. Park, W. J. Chang, C. W. Lee, S. Park, H.-Y. Ahn and K. T. Nam, *Nat. Energy*, 2017, **2**, 16185.

23 M. Ou, W. G. Tu, S. M. Yin, W. N. Xing, S. Y. Wu, H. J. Wang, S. P. Wan, Q. Zhong and R. Xu, *Angew. Chem., Int. Ed.*, 2018, **57**, 13570–13574.

24 Y. F. Xu, M. Z. Yang, B. X. Chen, X. D. Wang, H. Y. Chen, D. B. Kuang and C. Y. Su, *J. Am. Chem. Soc.*, 2017, **139**, 5660–5663.

25 H. W. Huang, H. F. Yuan, K. P. F. Janssen, G. Solis-Fernandez, Y. Wang, C. Y. X. Tan, D. Jonckheere, E. Debroye, J. L. Long, J. Hendrix, J. Hofkens, J. A. Steele and M. B. J. Roeffaers, *ACS Energy Lett.*, 2018, **3**, 755–759.

26 Q. L. Wang, L. M. Tao, X. X. Jiang, M. K. Wang and Y. Shen, *Appl. Surf. Sci.*, 2019, **465**, 607–613.

27 S. Park, W. J. Chang, C. W. Lee, S. Park, H. Y. Ahn and K. T. Nam, *Nat. Energy*, 2017, **2**, 8.

28 Y.-F. Xu, M.-Z. Yang, B.-X. Chen, X.-D. Wang, H.-Y. Chen, D.-B. Kuang and C.-Y. Su, *J. Am. Chem. Soc.*, 2017, **139**, 5660–5663.

29 M. Ou, W. Tu, S. Yin, W. Xing, S. Wu, H. Wang, S. Wan, Q. Zhong and R. Xu, *Angew. Chem., Int. Ed.*, 2018, **57**, 13570–13574.

30 Z. J. Li, E. Hofman, J. Li, A. H. Davis, C. H. Tung, L. Z. Wu and W. W. Zheng, *Adv. Funct. Mater.*, 2018, **28**, 7.

31 H. Y. Liu, Y. S. Tan, M. H. Cao, H. C. Hu, L. Z. Wu, X. Y. Yu, L. Wang, B. Q. Sun and Q. Zhang, *ACS Nano*, 2019, **13**, 5366–5374.

32 Y. X. Gao, X. Su, J. W. Zhang, H. W. Tan, J. H. Sun, J. Ouyang and N. Na, *Small*, 2021, **17**, 10.

33 Z. Long, Y. Wang, Q. Fu, J. Ouyang, L. He and N. Na, *Nanoscale*, 2019, **11**, 11093–11098.

34 Z. Guan, Y. Wu, P. Wang, Q. Zhang, Z. Wang, Z. Zheng, Y. Liu, Y. Dai, M.-H. Whangbo and B. Huang, *Appl. Catal., B*, 2019, **245**, 522–527.

35 G. Gao, Q. Xi, H. Zhou, Y. Zhao, C. Wu, L. Wang, P. Guo and J. Xu, *Nanoscale*, 2017, **9**, 12032–12038.

36 Y. Chen, R. Guo, X. Peng, X. Wang, X. Liu, J. Ren, J. He, L. Zhuo, J. Sun, Y. Liu, Y. Wu and J. Luo, *ACS Nano*, 2020, **14**, 6938–6946.

37 R. Hao, W. M. Sun, Q. Liu, X. L. Liu, J. L. Chen, X. W. Lv, W. Li, Y. P. Liu and Z. R. Shen, *Small*, 2020, **16**, 7.

38 M. V. Pavliuk, M. Abdellah and J. Sa, *Mater. Today Commun.*, 2018, **16**, 90–96.

39 J. Xu, S. Lai, D. Qi, M. Hu, X. Peng, Y. Liu, W. Liu, G. Hu, H. Xu, F. Li, C. Li, J. He, L. Zhuo, J. Sun, Y. Qiu, S. Zhang, J. Luo and X. Liu, *Nano Res.*, 2021, **14**, 1374–1381.

40 Y. Ren, C. Yu, X. Tan, H. Huang, Q. Wei and J. Qiu, *Energy Environ. Sci.*, 2021, **14**, 1176–1193.

41 H. Li, J. Shang, Z. H. Ai and L. Z. Zhang, *J. Am. Chem. Soc.*, 2018, **140**, 526–526.

42 L. M. Azofra, *Curr. Opin. Electrochem.*, 2022, 101073.

43 D. F. Yan, H. Li, C. Chen, Y. Q. Zou and S. Y. Wang, *Small Methods*, 2019, **3**, 21.

44 Y. Guo, J. X. Gu, R. Zhang, S. C. Zhang, Z. Li, Y. W. Zhao, Z. D. Huang, J. Fan, Z. F. Chen and C. Y. Zhi, *Adv. Energy Mater.*, 2021, **11**, 8.

45 Y. Deng, Z. Y. Xiao, Z. C. Wang, J. P. Lai, X. B. Liu, D. Zhang, Y. Han, S. X. Li, W. Sun and L. Wang, *Appl. Catal., B*, 2021, **291**, 8.

46 W. Liu, L. Han, H.-T. Wang, X. Zhao, J. A. Boscoboinik, X. Liu, C.-W. Pao, J. Sun, L. Zhuo, J. Luo, J. Ren, W.-F. Pong and H. L. Xin, *Nano Energy*, 2020, **77**, 105078.

47 F. L. Lai, W. Zong, G. J. He, Y. Xu, H. W. Huang, B. Weng, D. W. Rao, J. A. Martens, J. Hofkens, I. P. Parkin and T. X. Liu, *Angew. Chem., Int. Ed.*, 2020, **59**, 13320–13327.

48 L. Han, Z. Ren, P. Ou, H. Cheng, N. Rui, L. Lin, X. Liu, L. Zhuo, J. Song, J. Sun, J. Luo and H. L. Xin, *Angew. Chem., Int. Ed.*, 2021, **60**, 345–350.

49 X. Peng, Y. Mi, H. Bao, Y. Liu, D. Qi, Y. Qiu, L. Zhuo, S. Zhao, J. Sun, X. Tang, J. Luo and X. Liu, *Nano Energy*, 2020, **78**, 105321.

50 F. Li, G. F. Han, H. J. Noh, J. P. Jeon, I. Ahmad, S. S. Chen, C. Yang, Y. F. Bu, Z. P. Fu, Y. L. Lu and J. B. Baek, *Nat. Commun.*, 2019, **10**, 7.

51 W. Tong, B. L. Huang, P. T. Wang, Q. Shao and X. Q. Huang, *Natl. Sci. Rev.*, 2021, **8**, 10.

52 X. Guo, X. Y. Li, Y. C. Li, J. R. Yang, X. Wan, L. Y. Chen, J. Y. Liu, X. F. Liu, R. H. Yu, L. R. Zheng and J. L. Shui, *Nano Energy*, 2020, **78**, 9.

53 J. J. Li, Q. Q. Guan, H. Wu, W. Liu, Y. Lin, Z. H. Sun, X. X. Ye, X. S. Zheng, H. B. Pan, J. F. Zhu, S. Chen, W. H. Zhang, S. Q. Wei and J. L. Lu, *J. Am. Chem. Soc.*, 2019, **141**, 14515–14519.

54 H. Y. F. Sim, J. R. T. Chen, C. S. L. Koh, H. K. Lee, X. M. Han, G. C. Phan-Quang, J. Y. Pang, C. L. Lay, S. Pedireddy, I. Y. Phang, E. K. L. Yeow and X. Y. Ling, *Angew. Chem., Int. Ed.*, 2020, **59**, 16997–17003.

55 F. Calle-Vallejo, M. T. M. Koper and A. S. Bandarenka, *Chem. Soc. Rev.*, 2013, **42**, 5210–5230.

56 F. Wang and J. Mao, *Diamond Relat. Mater.*, 2021, **118**, 108494.

57 Y. Y. Tong, H. P. Guo, D. L. Liu, X. Yan, P. P. Su, J. Liang, S. Zhou, J. Liu, G. Q. Lu and S. X. Dou, *Angew. Chem., Int. Ed.*, 2020, **59**, 7356–7361.

58 P. S. Li, Z. Zhou, Q. Wang, M. Guo, S. W. Chen, J. X. Low, R. Long, W. Liu, P. R. Ding, Y. Y. Wu and Y. J. Xiong, *J. Am. Chem. Soc.*, 2020, **142**, 12430–12439.

59 Y. Gu, B. Xi, W. Tian, H. Zhang, Q. Fu and S. Xiong, *Adv. Mater.*, 2021, **33**, 2100429.

60 Y. Zhao, F. Li, W. Li, Y. Li, C. Liu, Z. Zhao, Y. Shan, Y. Ji and L. Sun, *Angew. Chem., Int. Ed.*, 2021, **60**, 20331–20341.

61 P. Li, S. Gao, Q. Liu, P. Ding, Y. Wu, C. Wang, S. Yu, W. Liu, Q. Wang and S. Chen, *Adv. Energy Sustain. Res.*, 2021, **2**, 2000097.

62 C. B. Zhu, Y. P. Fu and Y. Yu, *Adv. Mater.*, 2019, **31**, 25.

63 Y. W. Liu, M. Cheng, Z. H. He, B. C. Gu, C. Xiao, T. F. Zhou, Z. P. Guo, J. D. Liu, H. Y. He, B. J. Ye, B. C. Pan and Y. Xie, *Angew. Chem., Int. Ed.*, 2019, **58**, 731–735.

64 S. Fang, X. R. Zhu, X. K. Liu, J. Gu, W. Liu, D. H. Wang, W. Zhang, Y. Lin, J. L. Lu, S. Q. Wei, Y. F. Li and T. Yao, *Nat. Commun.*, 2020, **11**, 8.